Tests of demountable reinforced concrete slabs

Tests of demountable reinforced concrete slabs

Hanady Almahmood[1*], Ashraf Ashour[2], Diogo Figueira[3], Gurkan Yıldırım[4], Alper Aldemir[5] and Mustafa Sahmaran[6]

1 Assistant professor, Civil Engineering Department, Applied Science Private University, Amman, Jordan; Tel: 00962-790409743;

Email: h_almahmood@asu.edu.jo

[1] Postdoctoral research assistant, Civil Engineering Department, Faculty of Engineering and Informatics, University of Bradford, Bradford, West Yorkshire, BD7 1DP, UK Email address: h.a.a.a.almahmood@gmail.com

[2] Professor of Structural Engineering, Civil Engineering Department, Faculty of Engineering and Informatics, University of Bradford, Bradford, West Yorkshire, BD7 1DP, UK Email address: A.F.Ashour@bradford.ac.uk

[3] Post-doctoral Research Assistant, Faculty of Engineering & Informatics, University of Bradford, Bradford BD7 1DP, UK. E-mail: diogo_silva@hotmail.com.

[4] Associate Professor, Department of Civil Engineering, Hacettepe University, Ankara, Turkey. E-mail: gurkanyildirim@hacettepe.edu.tr

[5] Associate Professor, Department of Civil Engineering, Hacettepe University, Ankara, Turkey. E-mail: alperaldemir@hacettepe.edu.tr

[6] Professor, Department of Civil Engineering, Hacettepe University, Ankara, Turkey. E-mail: sahmaran@hacettepe.edu.tr

* Corresponding author Miss Hanady Almahmood,

Email: h_almahmood@asu.edu.jo

Abstract

This paper presents an experimental investigation of demountable reinforced concrete slabs using dry connections between reinforced concrete slab elements. The test specimens comprised six full-scale reinforced concrete slabs; one control slab monolithically cast, while the other five slabs were produced with mid-span demountable dry connections. The slab elements were cast separately and assembled using top and bottom steel plates joined to each side of the slab element by high tensile steel bolts with or without a shear key and embedded steel block. Theoretical analysis of the behaviour of the demountable slabs tested in comparison with the control specimen was also conducted.

The test results showed that using a dry connection consisting of a shear key at the assembled section is the most effective technique in terms of moment resistance, deflection, and flexural stiffness. On the other hand, the dry connection with embedded steel blocks failed prematurely because of stress concentration at the block edges. The moment capacity and deflection predictions of demountable slabs have reasonably correlated with the experimental results but required additional calibrated data from experiments.

Keywords: Demountable structures; Dry connections; Slabs; Reinforced concrete.

1. Introduction

Currently, at the end life of a structure, even though the materials remain usable, the structure is destroyed destructively, large steel parts are recycled by energy-intensive elements [1], while other materials are relatively recycled in low tech applications or landfilled, causing environmental and health issues and demanding a high cost. Therefore, the demountable concrete structures are considered a significant contribution to the current construction sustainability by creating high-quality and cost-effective structural systems. However, due to the limited research in this area, the current information in the literature about this topic is still rare.

There are mainly two approaches for assembling of precast concrete elements: namely semi-dry and dry connections. There are currently three types of semi-dry moment-resisting connections, achieved via content bars [2, 3], external U-wrap fibre reinforced polymer diagonal belt sheet [4] and dowel shear connections [5, 6]. However, semi-dry connections would not allow full demounting of structural elements after service life of structures as injected grouts or some parts of cast-in-situ concrete must be mechanically damaged and detached in addition to cutting the steel reinforcement during disassembly process, creating serious demolition waste. Additionally, since the semi-dry connection is still not distant in time most structures containing semi-dry concrete connections are still within their service life cycle, and the deconstruction/reconstruction has not been practiced yet [7].

On the other hand, the conducted research on demountable dry connections in reinforced concrete structures is still rare and limited. Only few connection solutions were investigated and tested in the literature, for example beam/column

[8-10], wall/wall and column/column [11, 12], wall/foundation and foundation/foundation [12, 13] and slab/slab connections [14].

Generally, beam/column connections are the most challenging dry-connections in precast reinforced concrete structures due to the bending and shear stresses transferred [15]. A limited number of beam/column dry connection investigations was conducted in the literature [8-10], proposing two solutions with a similar behaviour compared to the monolithic connection. On the contrary, wall/wall or column/column dry connections design is not as complex and challenging as beam/column connections. Those connections are primarily subjected to compression stresses, which can be simply transferred between the precast elements. Therefore, the compression in the connection mobilizes friction, and shear stress transfer is also enabled. Though, flexural stress is still existing between most connections of walls or columns. In this regard, only two proposals were found in the literature for wall/wall dry connections [11, 12], where a solution was achieved in which the failure occurred away from the connection zone, with a good ductility performance [12]. Moreover, a single solution was proposed for wall/foundation and foundation/foundation connections [12, 13], respectively where finite element models were developed to assess and verify their structural behaviour, but no experimental tests were conducted to verify their behaviour.

For slab/slab dry connections, the first study found in the literature proposed a shear key filled with aluminium foam, providing fire resistance and extra shear strength to the connection and insulation [14]. Push-off tests were conducted to evaluate the structural performance of the prestressed connection experimentally, mainly calculating the transferred shear stresses. However, this connection was not designed for flexural stress transfer. No further studies were found on similar connections to provide validation. Therefore, a new configuration

was recently proposed in which the connection is made by using top and bottom steel plates attached to the surfaces of the slabs [16]. The steel plates are then connected to the slabs by using threaded bolts anchored to the slab's segments. Although the proposed connection transfers flexural stresses through the steel plates, enhancement can still be made, mostly on the efficiency of the shear stress transfer. Furthermore, the proposed connection [16] has not been physically or computationally tested to confirm their behaviour and credibility.

To the knowledge of the authors, this is the first experimental investigation, aiming to achieve an improved solution for slab/slab joints in a typical reinforced concrete floor. In this research, four different dry coupling techniques are proposed, namely, simple screw coupling, screw coupling with shear key, bolted connection with steel embedded block, and bolted connection with a combination of shear key and steel embedded block. The shear key sewed by threaded bolts, and then the bolts are anchored on a steel plate that carries tension stress at the bottom surface of the slabs, similar to the solution presented earlier [16], but not tested. Another connection is also proposed, having on each slab an additional embedded steel block with ribs, welded to the steel reinforcement in tension at the bottom of the slabs. In this solution, the tensile stress is more easily transferred through the connection since it is directly transmitted from the reinforcement to the steel blocks. Such dry connection would facilitate the future reuse of slabs at the end of their life, potentially achieving a significant reduction in embodied energy of slabs as well as giving the clients the benefit of retaining the value of their assets.

Experimental programme

2.1 Test specimens

The test programme included six simply supported slabs. The reinforcement details and the dimensions of the tested specimens are shown from Fig.1 to Fig. 10. All slabs had a rectangular cross-section of 500 mm width by 160 mm depth. The total span length was 5200 mm, including a simply supported span of 5000 mm and two overhangs of 100 mm each. The main longitudinal and distribution slab reinforcements were the same for all specimens tested. Stainless steel bars were used as internal slab reinforcement because of their corrosion resistance. The main reason for selecting stainless steel is to enhance the durability of the slabs, allowing their reuse after dismantling at the end of life in real applications. FRP reinforcing bars were also a good candidate to be used in such slabs due to their excellent corrosion resistance; however, the difficulty in bending and welding to the end steel blocks at the two-slab element connection, made the stainless steel reinforcement more favourable. Five stainless steel deformed bars of Ø12 mm diameter were chosen as the main longitudinal slab reinforcement, as illustrated in Fig. 1-b. In addition, stainless steel deformed bars of Ø8 mm spaced at 150 mm at the bottom were chosen as lateral, distribution reinforcement.

The details of all tested specimens are summarized in Table 1. One specimen, the reference (REF) slab, was designed as a monolithic reinforced concrete slab for comparative purposes, as shown in Fig. 1. In contrast, the other five specimens were designed to be assembled using top and bottom steel plates connected by high-tensile strength bolts. Additionally, steel ducts were embedded into the slabs to hold the bolts at the correct connection positions.

The main parameter investigated in this experimental programme was the dry connection configuration between the two slab elements. Four different scenarios were used to connect the slabs: (1) simple bolted connection, (2) bolted connection with a shear key, (3) bolted connection with steel embedded block and (4) bolted connection with a combination of shear key and steel embedded block. The notation of the slabs was defined according to the connection details, as listed in Table 1. The first number in the notation specifies the number of bolts, while the second number indicates the diameter of the bolts. The third letter indicates whether the slab connection has a shear key, ‘K’, or not ‘NK’. Likewise, the fourth letter states the use of embedded steel blocks, ‘B’ for embedded steel blocks, and ‘NB’ for no embedded steel blocks.

Two specimens were designed without a shear key or embedded steel block, varying the diameter and the number of connecting bolts. The details of these slabs C-4-16-NK-NB and C-5-12-NK-NB are shown in Figs. 2 and 3. Each specimen included two identical segments; the length of each part was 2600 mm, as shown in Fig.2 (a). The front view of the two slabs before and after assembly is presented in Fig. 3. Specimen C-4-16-NK-B, shown in Fig. 4, was designed using embedded steel blocks to hold the bolt ducts. Those blocks were welded to the main longitudinal tensile reinforcement at the bottom of the slab segments, aiming to transfer the tensile stress more efficiently into the connection as it is directly transmitted from the reinforcement to the steel plates. The slab included two identical segments with a total length of 2600 mm. The dimensions and the details of the embedded steel block used in these slab segments are shown in Fig. 5(a). The front view of the two slab segments before and after assembly is shown in Fig. 6.

One specimen was designed with a shear key linked by threaded bolts at the mid-span section to enhance the shear stress transfer. The details of slab C-5-12-K-NB are shown in Fig. 7. The slab included two segments, one segment with top concrete step and one with bottom step, each of 100 mm width by 80 mm depth. The total length of each element, including the step, was 2650 mm, as shown in Fig. 7(a). In addition, stirrups were used around the bolt ducts of each slab segment to strengthen the connection section by providing concrete confinement, as shown in Fig. 7. The front view of the slab before and after the connection is shown in Fig.8. Finally, slab C-4-16-K-B was connected using a combination of a key and an embedded steel block. Two different sizes of steel blocks were used; a wider steel block 2 was used for the slab segment with a bottom concrete step to accommodate the two-bolt lines, as shown in Fig. 5(b). However, a steel block 1 with a smaller size was used for the slab segment with a top concrete step, where there was one line of bolts, as shown in Fig. 5(a). The details of reinforcement of C-4-16-K-B are shown in Fig. 9. The specimen included two segments; the total length of each element, including the step length, is 2650 mm. Fig. 10 shows the two segments before and after assembly.

2.2 Materials

Stainless steel bars were used for the main longitudinal and lateral reinforcement. Pull out tensile tests were carried out to assess the tensile properties of the reinforcement, as listed in Table 2.

Ready-mix geopolymer concrete was used to cast the specimen. The mix was designed to a target compressive strength of 35 MPa with a maximum aggregate size of 20 mm. The main ingredients of concrete were GGBS, alkali activators (sodium silicate and sodium hydroxide), coarse and fine aggregates as well as admixtures to enhance the concrete workability. The concrete compressive

strength for each test specimen was found by testing three cubes of 100 mm on the day of each slab test, while the splitting tensile strength was obtained by testing three concrete cylinders of 150 mm diameter by 300 mm height. The results of concrete properties are also presented in Table 3.

The connecting plates were made of 8 mm thickness stainless steel. Also, high tensile strength steel bolts of Grade 10.9 (tensile strength of minimum 1000 MPa and yield strength up to 900MP), high tensile nuts of Grade 10 (tensile strength of minimum 1000 MPa), and mid-steel ducts and washers were used for the connection.

2.3 Test setup

Two stainless steel plates of 500 mm width by 8 mm thickness were used to assemble the two parts of each slab. The plates were drilled at the position of the bolts before assembly. Afterward, they were placed at the top and the bottom surfaces of the slabs. The slabs were, then, bolted to each other using fully threaded bolts of 250 mm long, with a washer and nuts at each bolt ends. For consistency, the bolts were tightened using a torque wrench with an applied torque of 120 N.m on each bolt.

The slab test–rig setup is shown in Fig. 11. A 1000 kN hydraulic jack was used to test the slabs using a steel spreader beam to transfer the load to the two loading plates. The loading plates were set in position using special grout material to avoid any movement throughout the test. The slabs were supported using a roller support at one end and a hinge support at the other end. The top and bottom bearing plates were 150 mm width by 500 mm length to concrete the full-slab width.

Three digital cameras were used to measure the crack width; two were placed at the loading location, while one camera was focused on the mid-span section of

the slab. Moreover, seven linear variable differential transducers (LVDTs) were employed to track the deflection of the slabs during tests. Five LVDTs were placed under the slab to measure the deflection at different locations, while the top LVDTs set at the end supports measuring the system stability. Two strain gauges were attached to the stainless steel reinforcing bars under loading points before casting each slab segment to measure their strain, while two strain gauges were used externally at the center of the top and bottom of the connection steel plates. For concrete, special strain gauges were used at the top of the concrete section (compression side) to measure the concrete strain during the test. The load was applied to the slabs by displacement control where the displacement changed incrementally by 0.09 mm/sec. The measurement system of strain gauges, LVDTs, load cell, and the hydraulic jack were connected to the data logger to record the readings at every load increment during the test.

2. Experimental results

3.1 Crack propagation and modes of failure

The cracks of the tested slabs were outlined and recorded manually, as shown in Fig. 12. The first detectable crack was recorded at a total applied load of 3.0 KN for all slabs tested at the mid-span region between the two applied load points as all slabs had almost the same concrete tensile strength, resulting in a similar cracking moment. Considering elastic theory, the total cracking load P_{cr} for each slab may be calculated from:

$$P_{cr} = \frac{f_{ts} b h^2}{6a} \quad (1)$$

where f_{ts} is the flexural tensile strength of concrete, a is the shear span, b and h are the slab width and depth, respectively. The theoretical cracking loads obtained from the above formula are presented in Table 4, reasonably agreeing with the experimental cracking load of 3.0 kN. With increasing the applied load, many more vertical flexural cracks developed along the slab span, reducing the flexural stiffness of slab specimens. As the load increased, the width of existing cracks developed wider until the maximum travel capacity of the actuator of 200mm is reached when the loading process stopped. Such deflection (slab span/25) is considered excessive and would clearly violate the serviceability limit state criteria of structural design for deflection, that is generally limited to a ratio of slab (span/25).

Figs. 13 and 14 show the deformation shape and the recorded mode of failure for all slabs tested, respectively. The observed mode of failure for the REF slab started with flexural cracks at mid-span region. The recoded cracks extended slightly to the compression zone of the mid-span section. Conversely, there was no sign of concrete crushing because the slab was not tested to the maximum load capacity due to the limited travel capacity of the hydraulic jack. Steel yielding was recorded at 85% of the maximum total load ($\approx 36.5kN$).

Slabs C-4-16-NK-NB, C-5-12-NK-NB, and C-5-12-K-NB demonstrated tensile-flexural cracks initiated at the section where bolts were used due to stress concentration at the bolt location, as observed in Fig.14(b), (c), and (e), respectively. The dominant cracks, which were recorded along the lines of the connecting bolts, developed wider and more significantly with increasing the load. Those cracks started at the concrete holes and extended along the bolt line due to stress concentration and section reduction due to holes [17]; however, the slab

was not disintegrated due to the existence of the top and bottom steel plates holding the two slab segments together.

Conversely, specimens with embedded steel blocks, C-4-16-NK-B and C-4-16-K-B, exhibited an early premature failure due to the high-stress concentration at the block edges and the significant reduction of the concrete section due to the presence of the steel blocks. The failure of specimens was demonstrated by a wide crack at the embedded steel block edge, as seen in Fig. 14(d) and (f). Again, the existence of the top and bottom steel plates provided a well controlled failure and prevented a full disintegration of the two slab segments at the moment critical zone.

3.2 Crack width

The crack width at the slab soffit of the main crack against the total applied load is presented in Fig. 15, whereas the maximum crack width of the main crack at failure is listed in Table 4. The crack width was measured at the dominant crack of each specimen, recorded mainly at the area between the two-point loads. Generally, the width of the cracks of the demountable slabs was significantly larger than that of the REF slab due to embedded threaded bolts in concrete, that weekends the concrete section and causes tensile stresses concentration.

The crack width for slabs with the simple bolted connection, C-4-16-NK-NB and C-5-12-NK-NB, was almost the same until 75 % of the C-4-16-NK-NB maximum total load. However, at higher loads, a sudden increase in the crack width of specimen C-5-12-NK-NB was observed because of the more bolts used, resulting in a weaker concrete section. Slab C-5-12-K-NB, with a key connection, recorded the lowest value of crack width compared to other specimens owing to the improvement of the stiffness at the assembled section and the enhancement of

concrete compressive strength due to the confinement of concrete provided by the stirrups around the ducts in the vicinity of the connection.

On the other hand, slabs with embedded steel block connections showed the widest crack at failure compared to other specimens. However, Slab C-4-16-K-B exhibited a lower crack width than C-4-16-NK-B before the sudden failure due to the stiffness enhancement achieved by the shear key. Furthermore, both slabs recorded early failure identified by large crack width due to the high-stress concentration at the embedded block edge.

3.3 Strains in reinforcement, concrete, and steel-plates

The variation in the tensile strains in the stainless steel reinforcement with the total applied load is presented in Fig. 16. Generally, there was no significant difference between the recorded strain values of the stainless steel reinforcement of the demountable slabs at the same load owing to the fact that all slabs were reinforced with the same longitudinal reinforcement ratio, confirming that the demountable connection is able to achieve full continuity of the two slab segments. Slabs with embedded steel blocks, C-4-16-NK-B and C-4-16-K-B, exhibited premature failure; therefore, no steel yielding was recorded. However, steel yielding was recorded in the REF slab at 85% of the maximum total load, while no steel yielding was recorded in other demounted specimens. As the loading process has to be stopped at the limiting travel distance of the actuator, no steel yielding point could be reached. However, the wide cracks observed in most of demountable specimens may be related to bond between the stainless steel bars and concrete due to insufficient anchorage.

The measured strains in concrete against the total applied load is shown in Fig.17. The maximum-recorded strains in concrete at the mid-span section for all tested slabs did not reach or exceeded the theoretical crushing strain value of

0.0035 as all slabs were not tested to the maximum load capacity due to the limitation of the jack's travel capacity limitation.

The strains at the top and bottom steel connecting plates are presented in Fig.18. As expected, the top plates recorded compression strains while the bottom plates were under tensile strains; besides, no steel yielding was recorded before failure at both locations. The top and bottom steel plates of the slabs with a key connection, C-5-12-K-NB and C-4-16-K-B, showed the lowest strain values until failure, confirming the effectiveness of the key connection compared with others. Conversely, the demountable slab with embedded steel block and with no shear key, C-4-16-NK-B, exhibited the most significant strain values at both bottom and top steel plates due to the stress concentration at the embedded steel-block edges and the significant reduction of concrete section. Moreover, the bottom steel plates of specimens C-5-12-NK-NB and C-4-16-NK-NB showed reduction of tensile strains at higher loads due to the extra length of the bottom steel plate outside the bolt lines that did not follow the deformation of the slab bending, as observed in Fig.14(b) and (c).

3.4 Load capacity

The total load capacities of the slabs tested are presented in Table 4. Although the connected slabs were designed to be comparable to the REF Slab, the total load capacities of all connected slabs were lower than the REF slab due to stiffness reduction caused by the large crack width at the connection. The total load of the slabs with simple bolted connection, C-4-16-NK-NB and C-5-12-NK-NB, was lower than the REF slab by 31.7% and 41.2%, respectively.

The total load capacities of the slabs with embedded steel blocks, C-4-16-NK-B and C-4-16-K-B, were clearly the lowest of all specimens, resisting 42.3% and 38.7%, respectively, of the REF slab load capacity because of the stress

concentration at the embedded steel block, which caused an early failure of the tested slabs. Furthermore, the total load capacity of C-5-12-K-NB was 25.2% lower than the REF slab; however, it was the highest load compared to other demountable slabs, indicating the efficiency of using a shear key as a dry connection between slab segments.

3.4.1 Theoretical prediction of load capacity

The flexural moment capacity of the control slab tested may be predicted from the simplified rectangular stress distribution proposed by various codes of practice, for example the Structural Eurocodes (EC2) [18] considering strain compatibility and equilibrium of forces. In such case, the depth of the neutral axis x may be obtained from:

$$x = \frac{A_s f_y}{\lambda \eta f_{ck} b} \tag{2}$$

where A_s and f_y is the area and yield strength of the main longitudinal bottom steel, λ (=0.8 for $f_{ck} \leq 50MPa$) and η (=1.0 for $f_{ck} \leq 50MPa$) are two coefficients defining the effective height and effective strength of the simplified, equivalent rectangular stress distribution, respectively. Note that all partial safety factors for materials are assigned to 1.0. The slab moment capacity M_r is obtained from the resultant compression force in concrete or the tensile force in steel reinforcement as below:

$$M_r = A_s f_y (d - \frac{\lambda x}{2}) \tag{3}$$

where d is the slab effective depth. Therefore, the moment capacity of the control slab, REF obtained from Eqs. (2) and (3) is 40.16 kNm, agreeing well the experimental moment capacity of 42.9 kNm.

The presence of bolts in ducts and steel blocks introduces high stress concentration as well as reduction of the slab concrete section and the above approach seems un-realistic for predicting the capacity of demountable slabs tested. The slab section along the bolts is the weakest section of the slab, therefore, controlling the slab capacity as observed in the experiments. The forces in the top and bottom steel plates are in equilibrium and, therefore, equal, as shown in Fig. 19(a) and may be calculated from:

$$F_c = F_t = \frac{M_m}{z} \tag{4}$$

where F_c and F_t are the top and bottom forces in the steel plates, respectively, M_m is the moment at the mid-span section and z is the distance between the top and bottom steel plates. These forces are transferred to the slabs via the bolts, causing direct tensile forces on one side of the slab and compression on the other side, as shown in Fig. 19(b). Therefore, the tensile stresses f_t in concrete caused by the bolts may be calculated from:

$$f_t = \frac{F_t}{A_{net}} \tag{5}$$

where A_{net} $(= (b - n\phi)h)$ is the net section area of concrete (see Fig.19 (c)), b and h are the width and depth of the slab, n and ϕ is the number and diameter of ducts, respectively. Considering Eqs. (4) and (5), the moment capacity M_r of the slab section may be calculated when the tensile stresses f_t reach the concrete tensile strength f_{ts}:

$$M_r = F_t z = f_{ts} A_{net} z \tag{6}$$

Table 4 presents the ratio of the experimental to predicted moment capacities as obtained from Eq. (6). It is to be noted that the net section area of slabs with

internal steel block, as shown in Fig.19(d), was reduced by 30% to reflect the presence of the steel block inside concrete that significantly reduced the concrete resistance. Overall, the prediction from Eq. (6) shows a reasonable agreement with the experimental moment/load capacities.

3.5 Load-deflection response

Fig. 20 demonstrates the deflection curve along each slab span, measured at a total load of 15 KN. This value was chosen because the minimum recorded load capacity for the tested slabs was 16.6 KN, allowing deflection profile comparison for all slabs tested. The results show that the critical deflection of the slabs was recoded at the mid-span section for all tested specimens. Consequently, mid-span measurements were used to plot the relationship between the total applied loads against the deflection of the tested slabs, as shown in Fig. 21. The top LVDTs readings at end supports were not presented because no settlement was recorded.

The load-deflection relationship started with linear load-deflection behaviour until cracking, which was recorded at 3 kN of the total load for all tested slabs. After cracking, all tested slabs exhibited a clear reduction in the flexural stiffness. As the load increased, there was a further decrease in the REF slab stiffness until the steel has yielded, as was recorded by the strain gauge. However, there was an additional stiffness drop for the demountable slabs compared with the REF slab. The flexural stiffness of the demountable slabs was diverse based on the connection technique. Slabs with simple bolted connection, C-4-16-NK-NB and C-5-12-NK-NB, exhibited almost similar stiffness until 75% of the maximum total load of slab C-4-16-NK-NB. Then, slab C-5-12-NK-NB showed more reduction than C-4-16-NK-NB, which might be the effect of using more bolts.

Alternatively, the slabs with a shear key at the connection, C-5-12-K-NB and C-4-16-K-B, showed enhanced stiffness compared to other specimens without a shear key due to the improvement in the shear resistance and the confinement of concrete provided by the stirrup. However, slabs with embedded steel blocks, C-4-16-K-B and C-4-16-NK-B, showed early failure because of the stress concertation at the embedded steel blocks. It is worth noting that slabs with embedded steel blocks (C-4-16-K-B and C-4-16-NK-B) exhibited softening phase after the early failure as demonstrated by the load-deflection curve (Fig. 21), internal steel reinforcement strains (Fig. 16), concrete strains (Fig. 17) and steel plates strains (Fig. 18). Such controlled failure signifies the role of the top and bottom steel plates after concrete failure in promoting ductile behaviour of the proposed demountable connections. Other slabs did not exhibit softening phase as the tests stopped due to the large deflections occurred in the slabs tested.

3.5.1 Theoretical prediction of load-deflection

The mid-span deflection Δ of one span slab under two-point loads, similar to the slab tested, is estimated from Eq. (7), below:

$$\Delta = \frac{Pa\,(3L^2 - 4a^2)}{24E_c I_e} \tag{7}$$

where P is the span load, a is the distance between the support and loading point, L is the span length, E_c is the modulus of elasticity of concrete ($\approx 4700\sqrt{f_c'}$; f_c' is the cylinder concrete compressive strength in MPa) and I_e is the effective moment of inertia of the concrete cross-section. The effective moment I_e of inertia is equal to the gross moment of inertia, I_g, before cracking (Eq. (8)), while it can be expressed by Eq. (9) after cracking [19].

$$I_e = I_g \qquad M_a \leq M_{cr} \tag{8}$$

$$I_e = \frac{I_{cr}}{1 - \left(1 - \frac{I_{cr}}{I_g}\right)\left(\frac{M_{cr}}{M_a}\right)^2} \leq I_g \qquad M_a > M_{cr} \tag{9}$$

where I_{cr} is the cracked moment of inertia, obtained from elastic analysis of the transformed cracked section, M_a is the applied moment and M_{cr} is the cracked moment of the section (= $f_{ts}I_g/y$, f_{ts} is the concrete tensile strength, y is the distance from the centroid of the gross section to tension face, neglecting reinforcement).

For the REF slab, the mid-span deflection can be estimated from Eq. (7) and either Eq. (8) or (9), depending on the applied moment, M_a. However, for demountable slabs, the full continuity of the slab slope at mid-span section is not fully satisfied by the top and bottom steel connecting plates, allowing a limited rotation occurring at mid-span section, as shown in Fig. 22. However, the rotations at the left- and right-hand sides of mid-span section are the same but opposite to each other due to symmetry. The amount of rotation is mainly controlled by the demountable connection detailing; for example the rigidity of steel plates, connecting bolts and cracks in the vicinity of the demountable connection. Therefore, the mid-span deflection of slabs with demountable connections may be calculated from Eq. (10):

$$\Delta = \frac{Pa\,(3L^2 - 4a^2)}{24E_cI_e} + \theta_m\frac{L}{2} \tag{10}$$

where θ_m is the rotation at midspan to the left or right of the demountable connection, as shown in Fig. 22.

To use Eq. 10 for the prediction of demountable slab deflection, the mid-span rotation value, θ_m, was adjusted for each slab's serviceability limit state (≈ 70% of the total load capacity of the slab) as explained below. The mid-span rotation, θ_m , was initially found for each load value up to 70% of the total load capacity by

substituting the experimental deflection values for the theoretical mid-span deflection, Δ in Eq. (10). The mid-span rotation results were, then, plotted against the total experimental load to find the best line fit between the experimental load and rotation value, as shown in Fig. 23 and listed in Table 5.

The variation between the obtained results was noticeable owing to the difference in stiffness of various connections adopted. The rotation value for demountable slabs with key, C-5-12-K-NB, was the lowest among the tested specimens, implying that adding a shear key to the assembled section enhanced the flexural stiffness and reduced the rotation value of slabs segments, agreeing with the experimental results. The validity of the linear regression was tested by finding the Pearson correlation test to measure the linear correlation between the experimental load and the mid-span rotation by using SPSS software, as listed in Table 6. Pearson correlation measures the strength of the linear relationship between two variables. It has a value between (-1 to 1), where a value of (-1) means a negative linear correlation. In contrast, a value of (0) indicates no correlation, and + 1 represents a total positive correlation. As seen in Table.6 Pearson correlation coefficients between the two variables were (0.862 to 0.99), indicating that the linear correlation between the two variables is statistically significant, and the linear regression model can be assumed as a good model for all datasets.

Although the dry connection rotation was different for each slab, the results showed a small variation. Therefore, the mid-span rotation, θ_m , value was projected to be the average value of the slopes, as calculated by Eq. 11.

$$\theta_m = \frac{2P}{994} \tag{11}$$

Fig. 24 shows a comparison between the predicted and the experimental load-deflection at the mid-span of slabs tested. For the REF slab, the predicted results using Eq. 7 were almost in good agreement with experimental results until 70% of the total load capacity of the slab (satisfying the serviceability limit state of design), as shown in Fig. 24(a). However, using the same equation significantly underestimated the predicted deflection at higher load values.

For the demountable slabs, Eq. 7 drastically underestimated the predicted deflection because of the assumption of continuity of the slab slope at the mid-span section. Therefore, the prediction calculated by Eq. (10) was approximately fitted to the experimental deflection by using the adjusted mid-span rotation values determined by Eq. (11). As a result, there is a better agreement between the experimental results and the deflection prediction using Eq. 10, as shown in Fig. 24, confirming the applicability of the proposed equations (10 and 11) to predict the deflections of demountable slabs.

3. Conclusions

The feasibility of demountable reinforced concrete slabs using dry connections between slab elements has been investigated in this paper, aiming to set future sustainable developments of reinforced concrete slabs in typical floor system. It mainly provides a proof-of-concept investigation for a sustainable structural concrete system.

The main elements of the proposed demountable connections include steel plates and bolts with or without a shear key and an embedded steel block. Five large-scale simply supported slabs with demountable/dry connections at mid-span section as well as a control specimen were tested and analysed. Theoretical prediction of the behaviour of the demountable slabs tested in comparison with

the control specimen was also presented. The following conclusions can be drawn based on the results obtained:

- Slabs without embedded steel block, C-4-16-NK-NB, C-5-12-NK-NB, and C-5-12-K-NB, failed due to cracks extended along the bolt line due to stress concentration and concrete section reduction due to holes. However, the slabs did not reach the maximum load capacity due to the limited actuator travel capacity but significantly exhibited unsatisfactorily excessive deflection.
- Conversely, specimens with embedded steel blocks, C-4-16-NK-B and C-4-16-K-B, exhibited excessive wide cracks at the embedded steel block edge, causing a premature failure due to the high-stress concentration at the block edge and concrete section reduction due to holes and existence of steel blocks.
- The slab with a dry connection consisting of a shear key at the assembled section exhibited the largest load-capacity and flexural stiffness, and least deflection and crack width.
- The slabs with a dry connection having embedded steel blocks prematurely failed because of stress concentration at the block edge as well as the significant reduction of concrete section.
- The moment capacity prediction of demountable slabs has shown a good agreement with the experimental results, emphasising the significance of various elements of demountable dry connections.
- The deflection prediction of demountable slabs using the proposed equations has also shown a good agreement with experimental results. However, this required additional calibration data for mid-span slope at various demountable connections.

Data Availability

The raw/processed data required to reproduce these findings cannot be shared at this time as the data also forms part of an ongoing study.

Acknowledgments

This work was supported by an Institutional Links grant, ID 414633184, under the Newton-Kâtip Çelebi Fund partnership. The grant is funded by the UK Department for Business, Energy and Industrial Strategy and TÜBİTAK – Scientific and Technological Research Council of Turkey and delivered by the British Council. For further information, please visit www.newtonfund.ac.uk.

Statements and Declarations

4. References

1. Gomer, C.R., et al., The feasibility of recycling activated steel first wall/blanket materials from fusion reactors. Fusion engineering and design, 1990. 11(4): p. 423-440.
2. Xiao, J., T. Ding, and Q. Zhang, Structural behavior of a new moment-resisting DfD concrete connection. Engineering Structures, 2017. 132: p. 1-13.
3. Yan, Q., T. Chen, and Z. Xie, Seismic experimental study on a precast concrete beam-column connection with grout sleeves. Engineering Structures, 2018. 155: p. 330-344.
4. Djamaluddin, R. Effect of diagonal belt to the moment capacity of the precast beam-column joint using CFRP sheet. in World Symposium on Civil Engineering. 2017. WSCE.

5. Belleri, A., et al., Seismic performance of precast industrial facilities following major earthquakes in the Italian territory. Journal of Performance of Constructed Facilities, 2014. 29(5).
6. Metelli, G., C. Beschi, and P. Riva, Cyclic behaviour of a column to foundation joint for concrete precast structures. European Journal of Environmental and Civil Engineering, 2011. 15(9): p. 1297-1318.
7. Ding, T., et al., Experimental and numerical studies on design for deconstruction concrete connections: An overview. Advances in Structural Engineering, 2018. 21(14): p. 2198-2214.
8. Aninthaneni, P.K., et al. Experimental investigation of dry beam-column moment connections for demountable precast concrete frame buildings. in New Zealand Society for Earthquake Engineering Annual Conference (NZSEE). 2016.
9. Navarro-Rubio, J., P. Pineda, and A. García-Martínez, Sustainability, prefabrication and building optimization under different durability and re-using scenarios: Potential of dry precast structural connections. Sustainable Cities and Society, 2019. 44: p. 614-628.
10. Kang, T. and D.J. Lee. Special Precast Beam-Column Connection Using Pure Dry Cast Method. in The 2013 World Congress on Advantages in Structural Engineering and Mechanics (ASEM 13): Jeju, Korea. 2013.
11. Colombo, A., et al., Design guidelines for wall panel connections. 2016: Publications Office.
12. Sun, J., H. Qiu, and Y. Lu, Experimental study and associated numerical simulation of horizontally connected precast shear wall assembly. The structural design of tall and special buildings, 2016. 25(13): p. 659-678.
13. Sabitov, L., et al. Development and investigation of the stressed-deformed state of the demountable foundation for support. in IOP Conference Series: Materials Science and Engineering. 2017. IOP Publishing.
14. Reinhardt, H.W. and G. Weiss. Demountable concrete structures with aluminium foam as joint material. in PRO 41: International RILEM Symposium on Environment-Conscious Materials and Systems for Sustainable Development. 2005. Vol. 41, RILEM Publications.
15. fib, Structural connections for precast concrete buildings. 2008, fib Bulletin 43, fédération internationale du béton.
16. Aninthaneni, P.K. and R.P. Dhakal. Demountable precast RC frame building system for seismic regions. Proceedings of the International Conference on Earthquake Engineering and Seismology (IZIIS-50). 2016. Christchurch (New Zealand).

17. Cai, G., et al., A Demountable Connection for Low-Rise Precast Concrete Structures with DfD for Construction Sustainability-A Preliminary Test under Cyclic Loads. Sustainability, 2019. 11(13): p. 3696.
18. EuroCode2, 2, Design of concrete structures-Part 1-1: General rules and rules for buildings, BS EN 1992-1-1: 2004. British Standards (BSi), 2004.
19. Bischoff, P.H., Deflection calculation of FRP reinforced concrete beams based on modifications to the existing Branson equation. Journal of Composites for Construction, 2007. 11(1): p. 4-14.

5. Figures

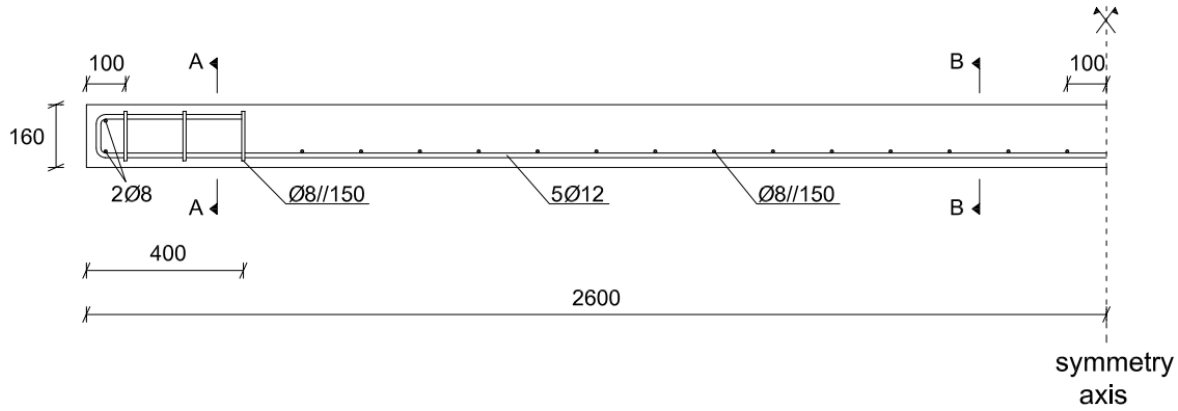

a. Longitudinal reinforcement details section.

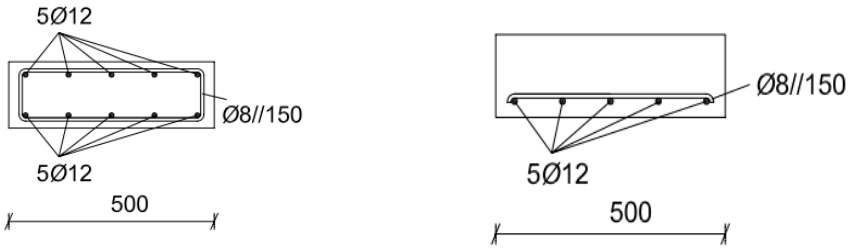

b. Side view A-A

c. Side view B-B

Figure 1: Reinforcement details of REF (reference) slab.

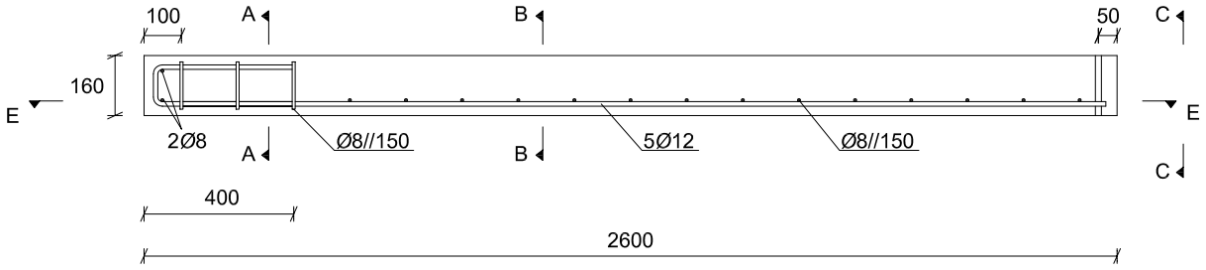

a. Front view

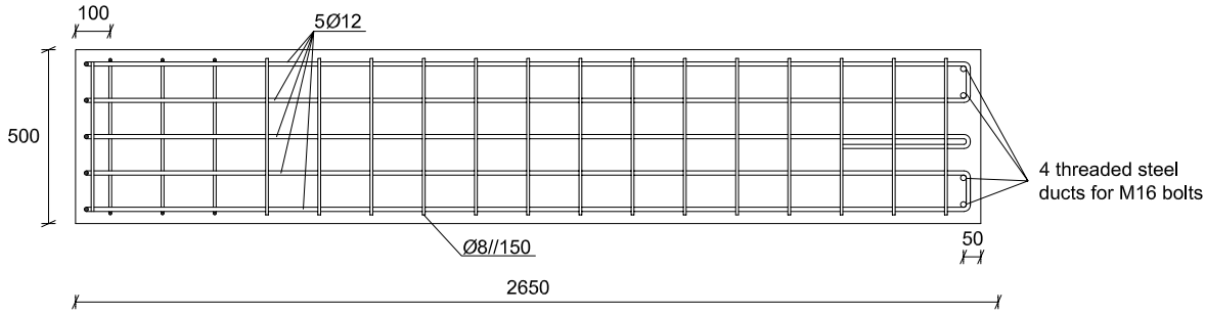

b. Top view E-E of C-4-16-NK-NB

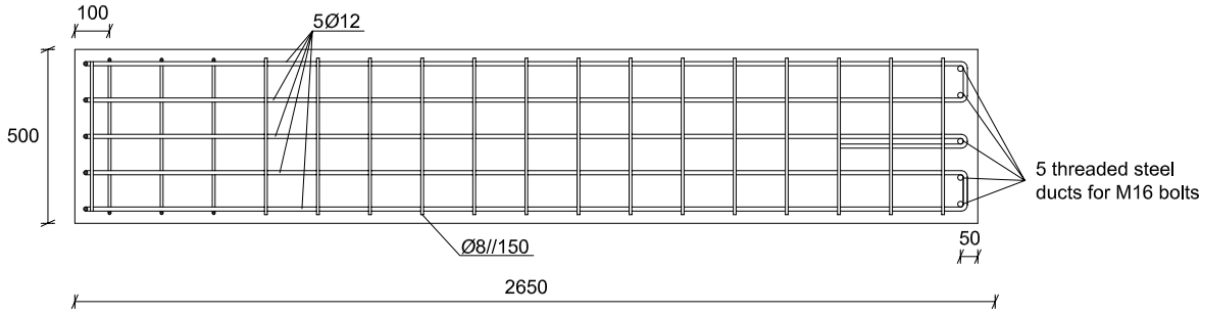

c. Top view E-E of C-5-12-NK-NB

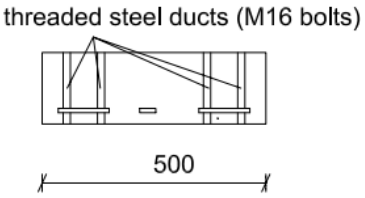

d. Side view C-C of C-4-16-NK-NB

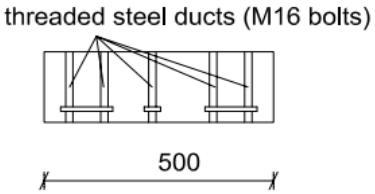

e. Side view C-C of C-4-16-NK-NB

Figure 2: Reinforcement details for slabs with no key nor embedded block.

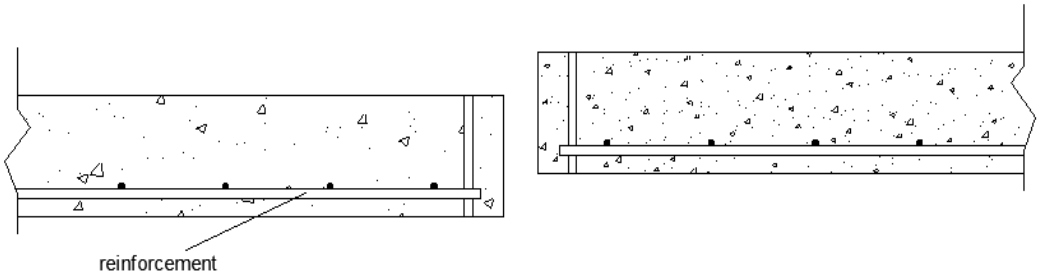

a. Before assembly

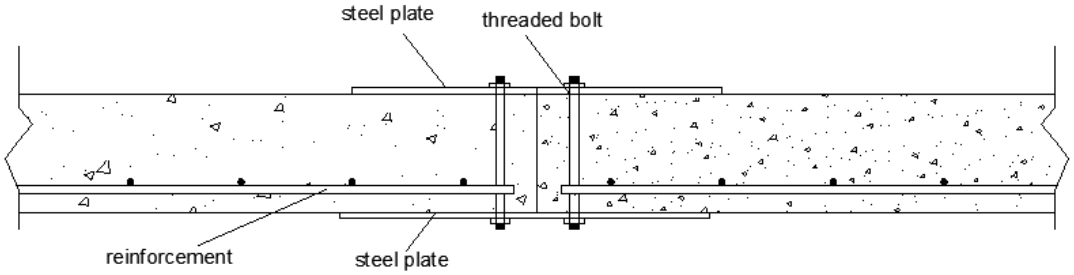

a. After assembly

Figure 3: Connection details with no key nor embedded block.

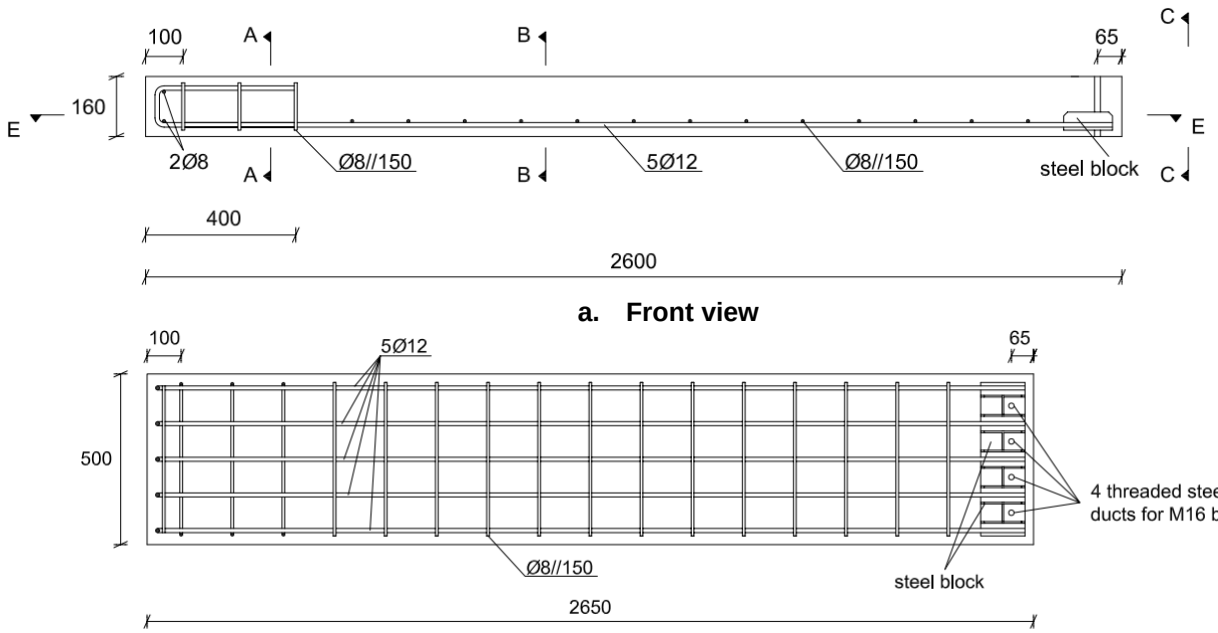

a. Front view

b. Top view E-E

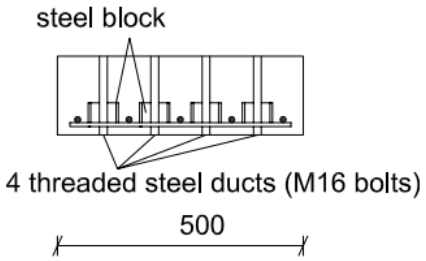

c. Side view C-C

Figure 4: Reinforcement details of slab C-4-16-NK-B (with embedded block but no key).

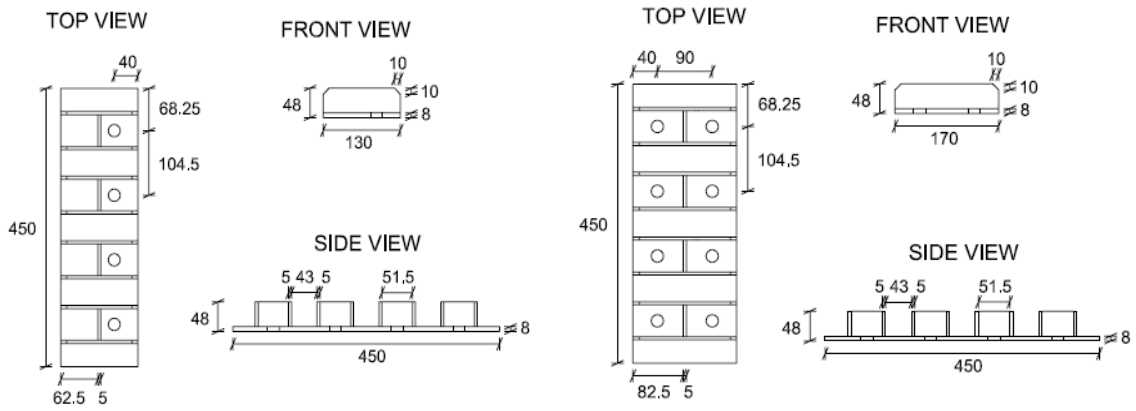

a. **Steel block 1** b. **Steel block 2**

Figure 5: Details of embedded steel blocks.

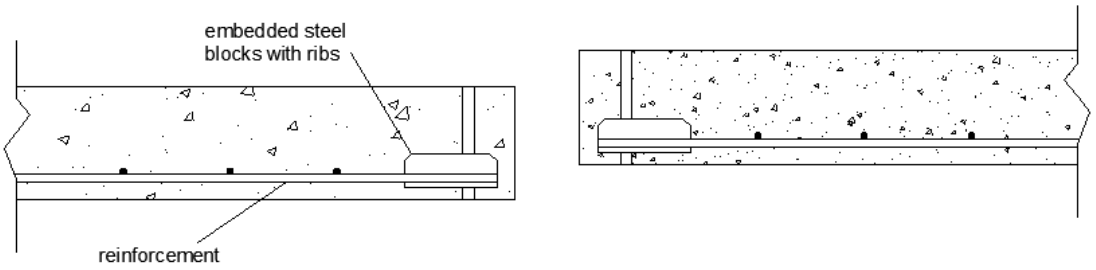

a. **Before assembly**

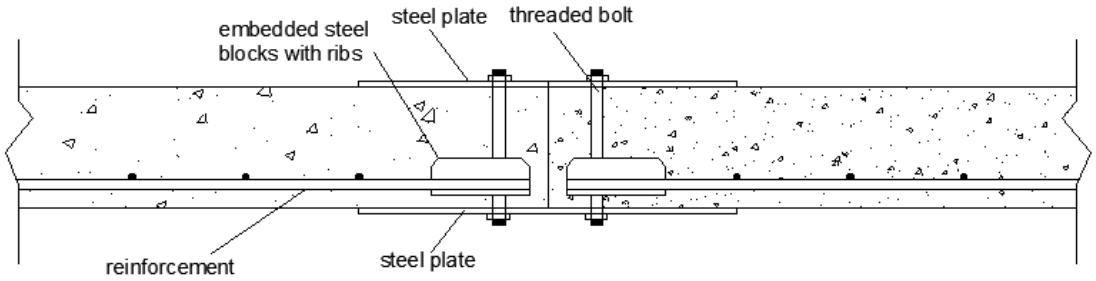

b. After assembly

Figure 6: Connection details of the slab with embedded block but no key.

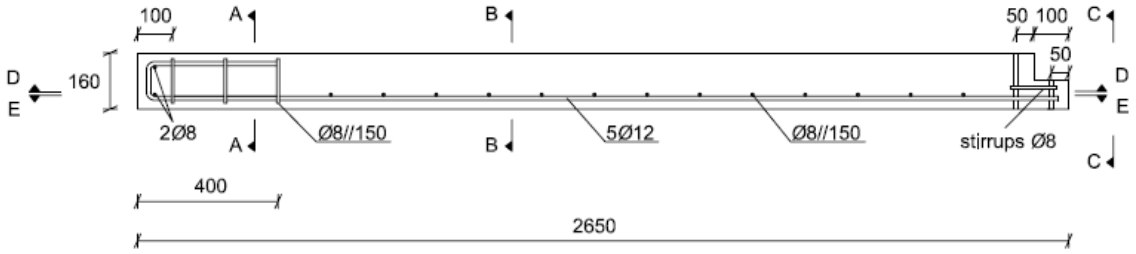

a. Front view for bottom step

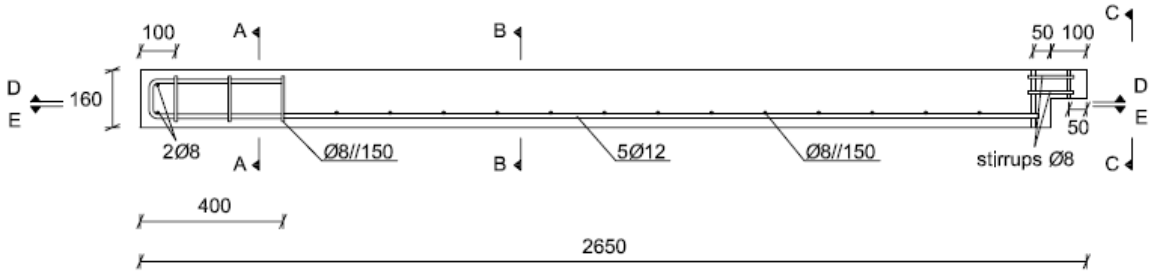

b. Front view for top step

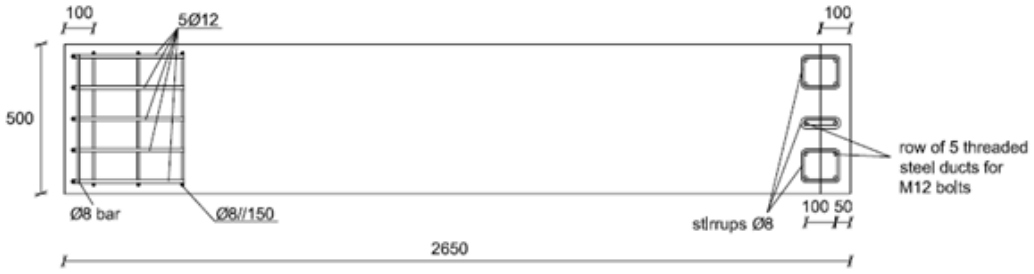

c. Top view D-D

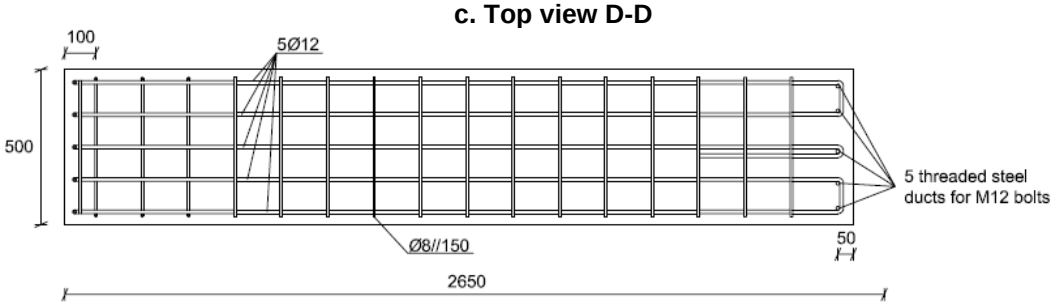

d. Top view E-E

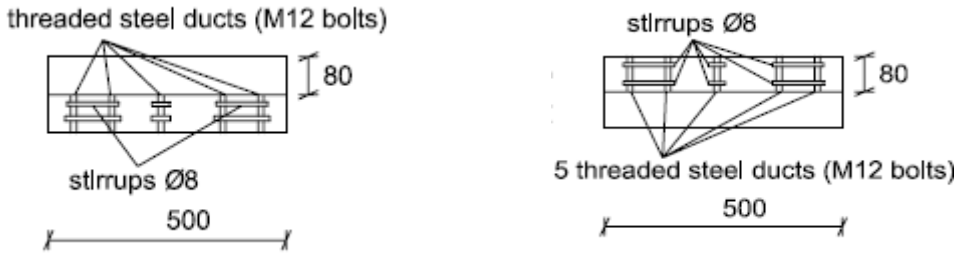

e. Side view C-C of bottom step **f. Side view C-C of top step**

Figure 7: Reinforcement details of C-5-12-K-NB (with a key but no embedded block).

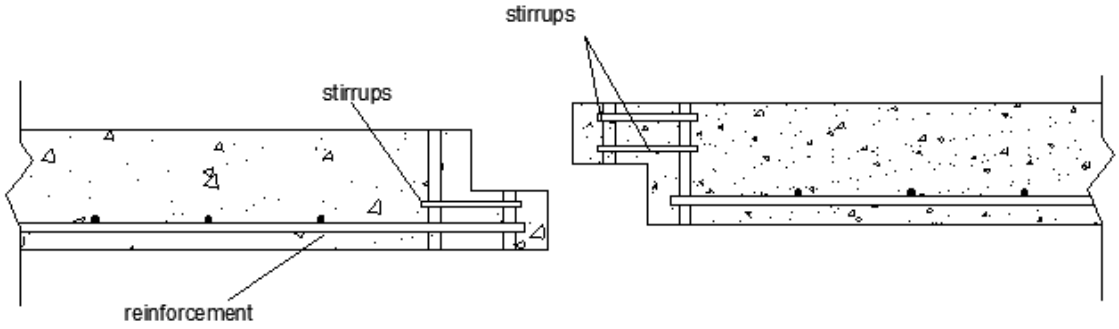

a. Before assembly

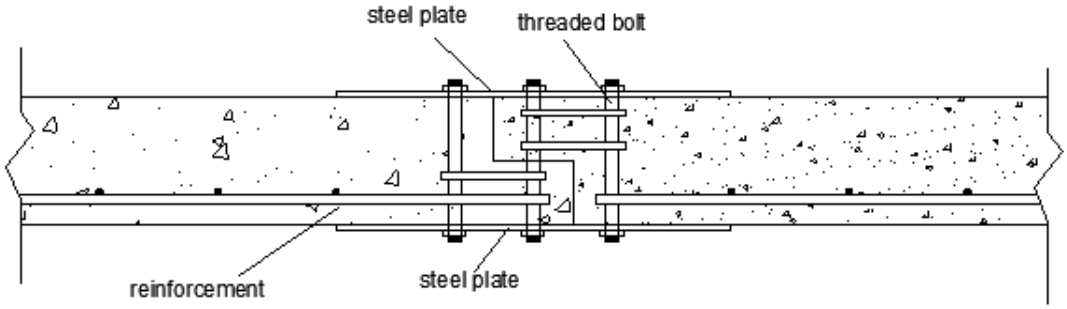

b. After assembly

Figure 8: Connection details of the slabs connected with a key and no embedded block.

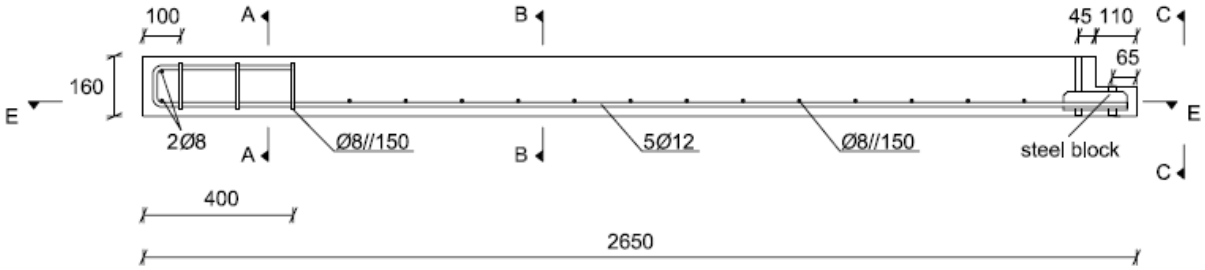

a. Front view of bottom step.

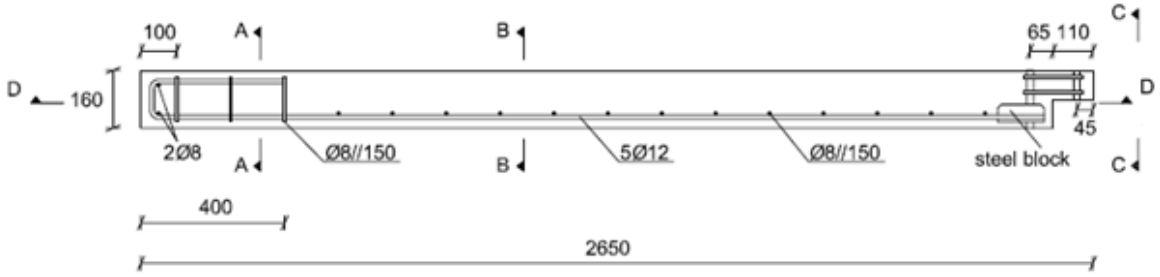

b. Front view of top step.

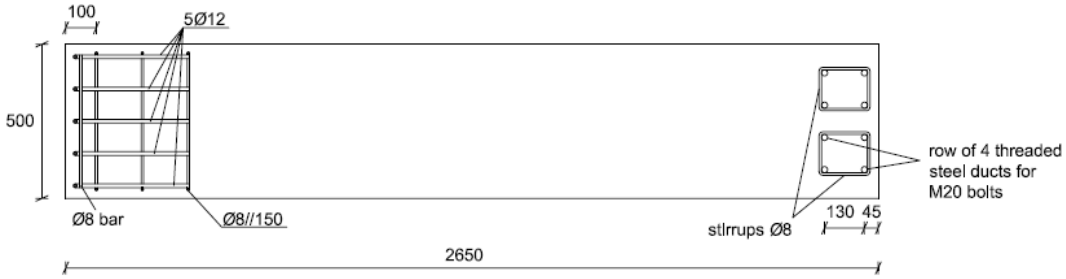

c. Top view D-D.

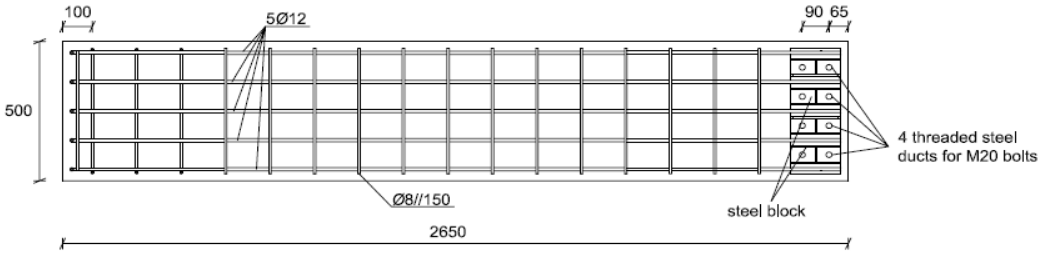

d. Top view E-E.

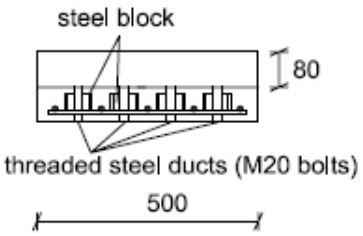

e. Side view C-C (bottom step)

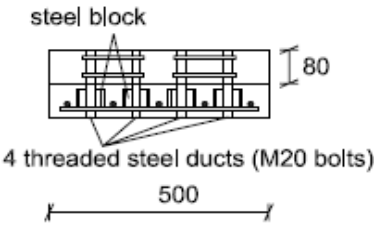

f. Side view C-C (top step)

Figure 9: Reinforcement details of C-4-16-K-B (with a key and embedded blocks).

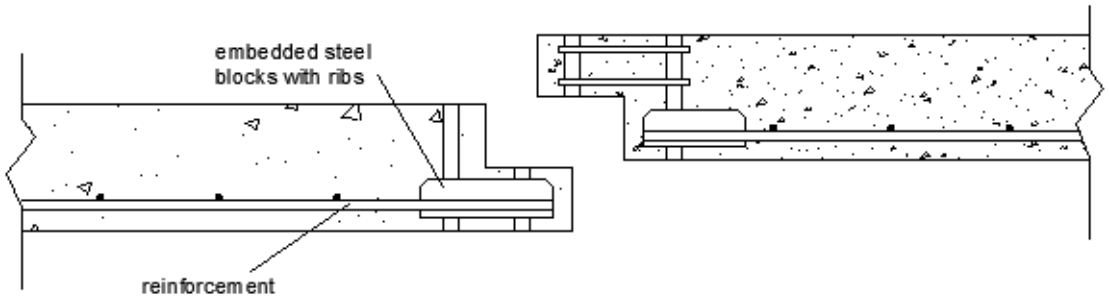

a. Before assembly

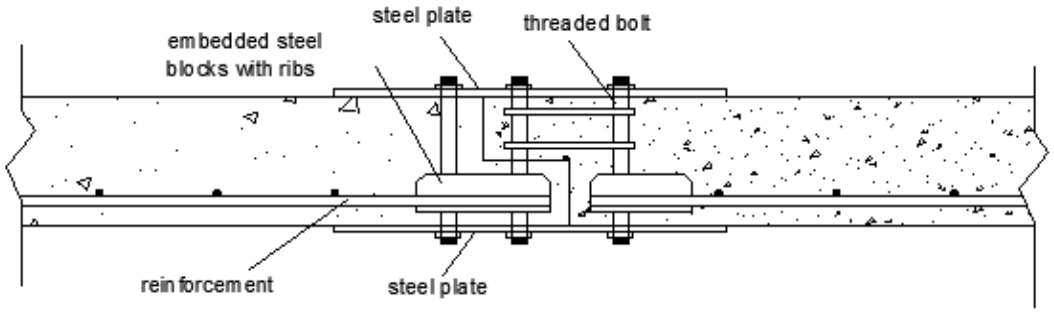

b. After assembly

Figure 10: Connection details of the slabs Connected with a key and an embedded block.

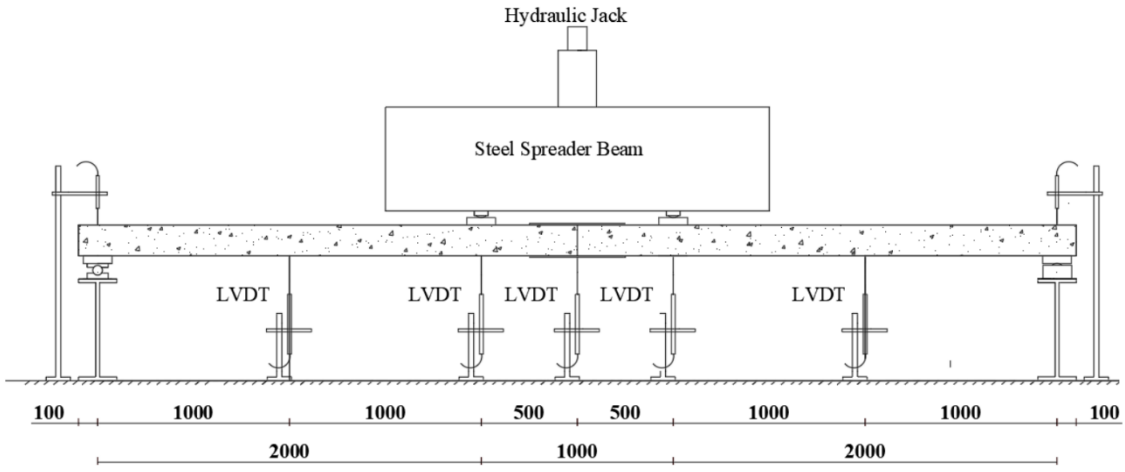

Figure 11: Experimental slab test setup (Dimensions in mm).

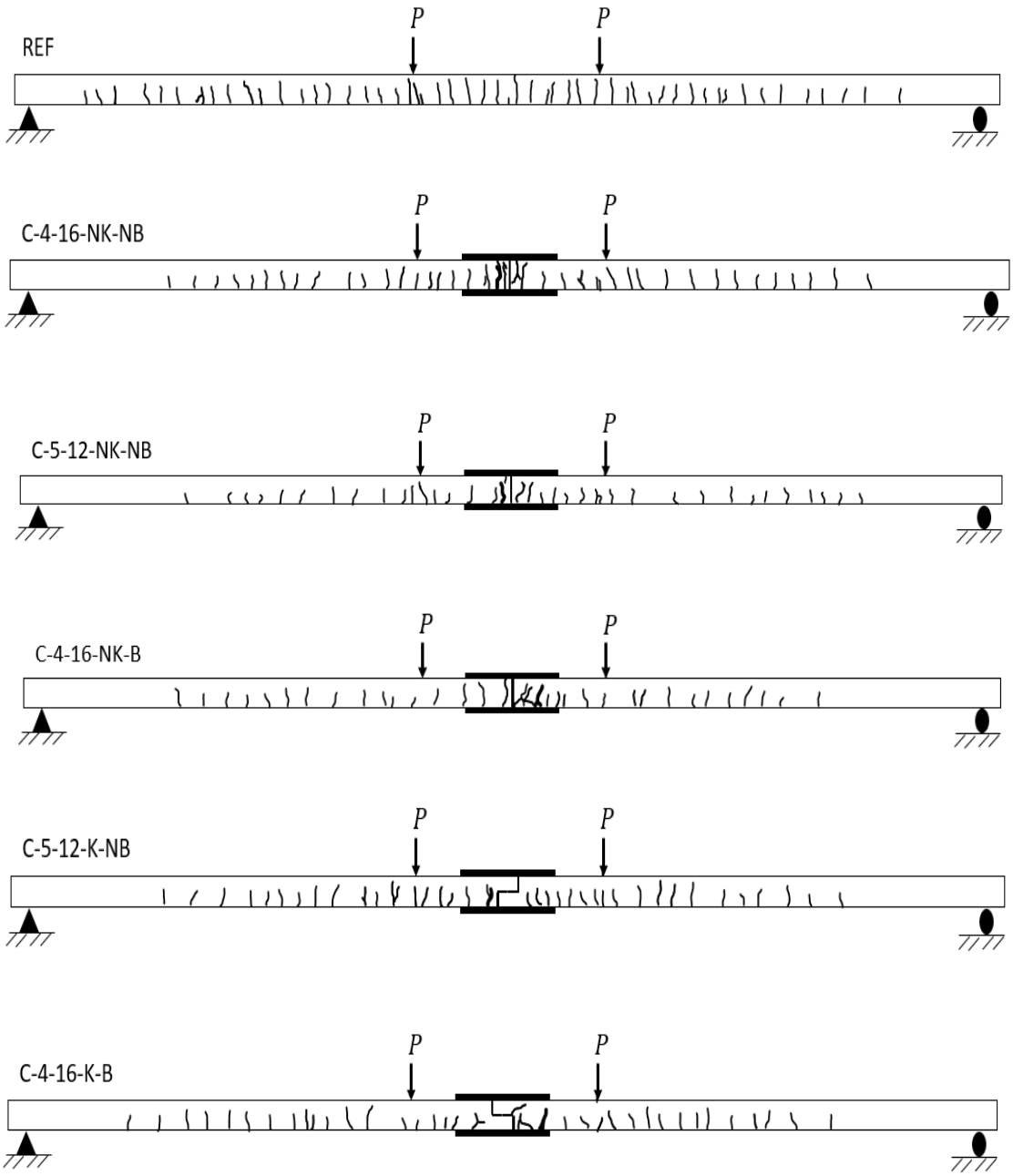

Figure 12: Crack patterns for the tested slabs at failure.

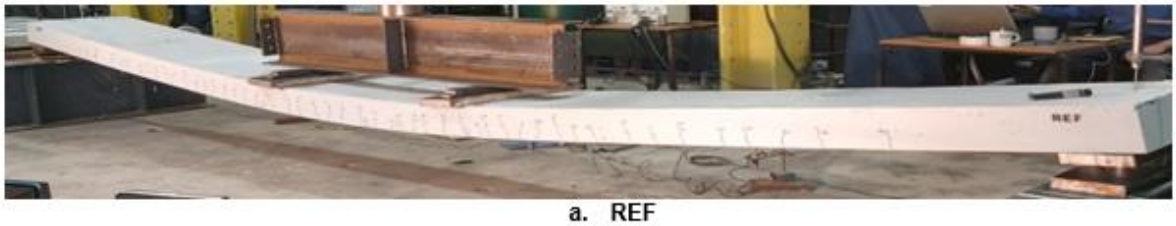

a. REF

b. C-4-16-NK-NB

c. C-5-12-NK-NB

d. C-4-16-NK-B

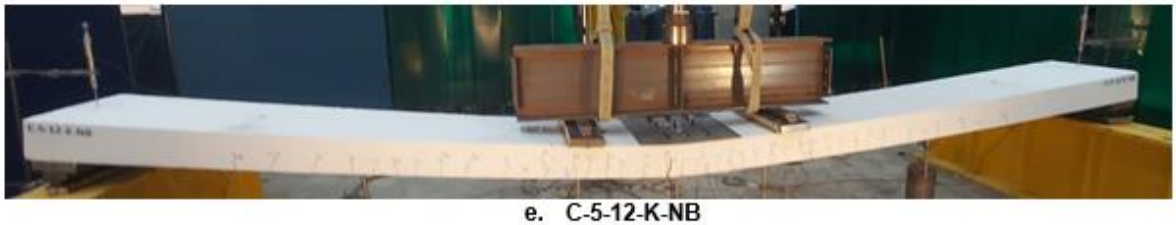

e. C-5-12-K-NB

f. C-4-16-K-B

Figure 13: Deformation shape of the tested slabs at failure.

a. REF

(Front) (Top)

b. C-4-16-NK-NB

c. C-5-12-NK-NB

d. C-4-16-NK-B

e. C-5-12-K-NB

f. C-4-12-K-B

Figure 14: Modes of failure of the tested slabs.

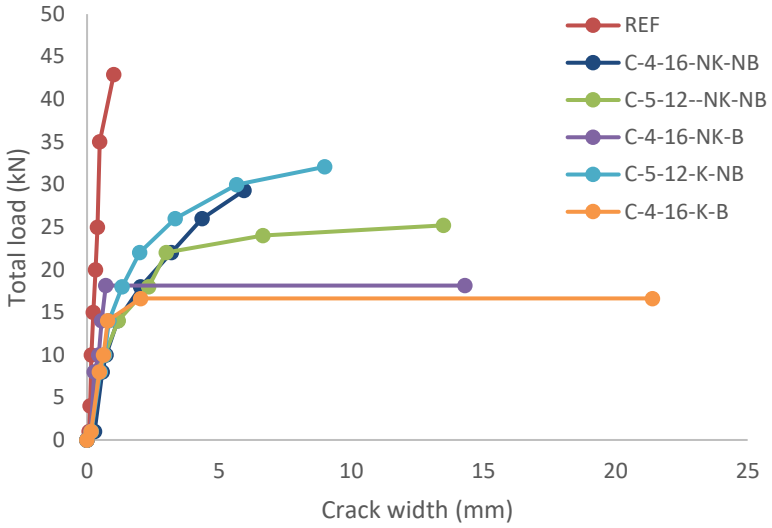

Figure 15: Dominant crack width of the tested slabs at the mid-span section.

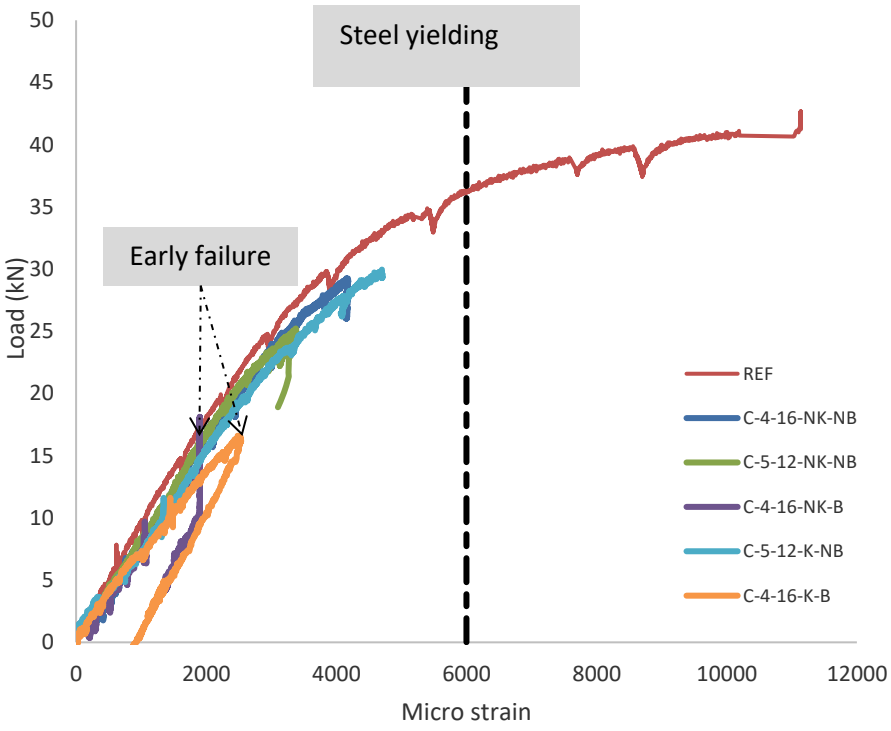

Figure 16: Variation of steel strains under loading point.

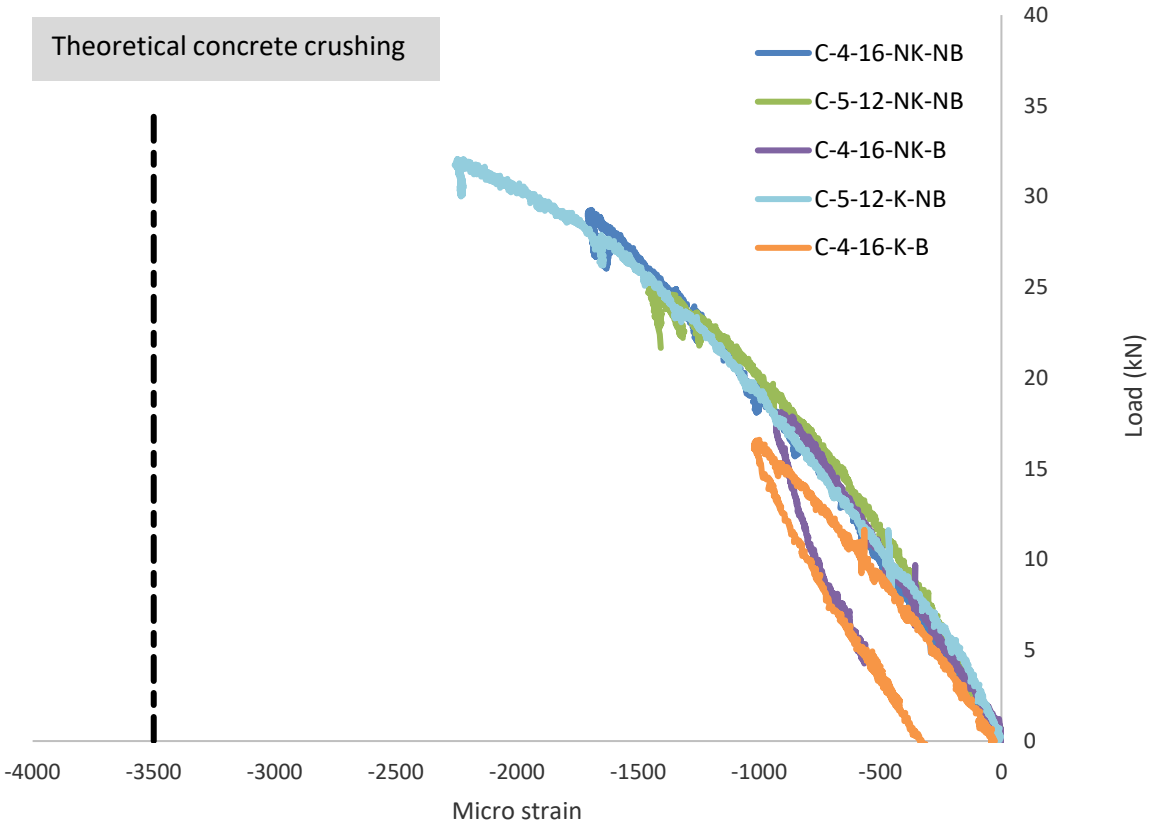

Figure 17: Variation of concrete strains at the top section of the tested slab.

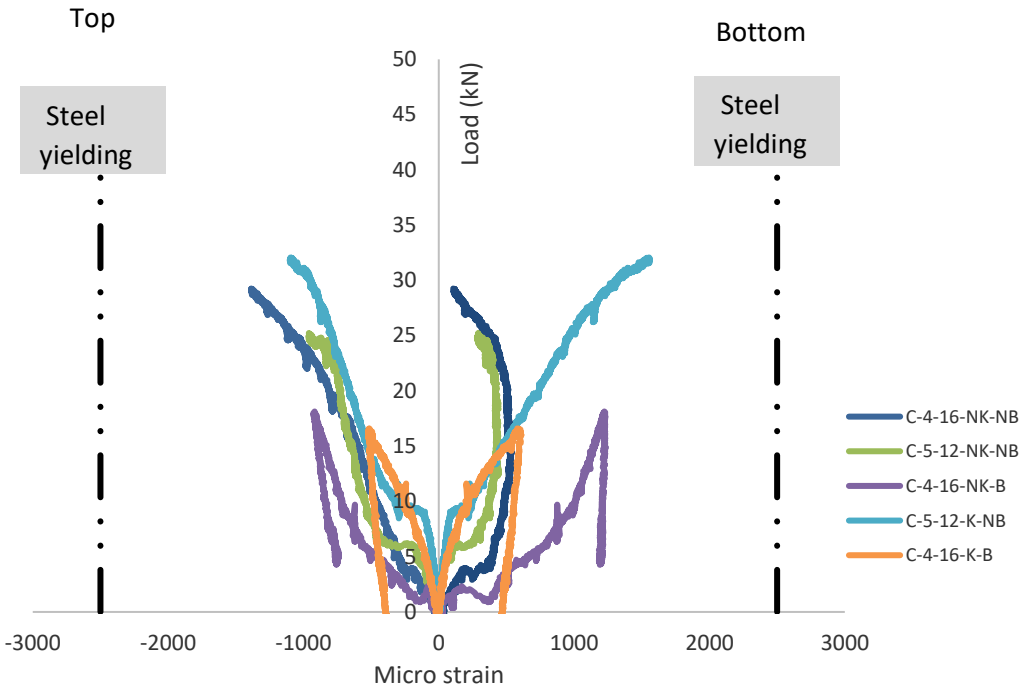

Figure 18: Variation of steel strains at the top and bottom steel plates .

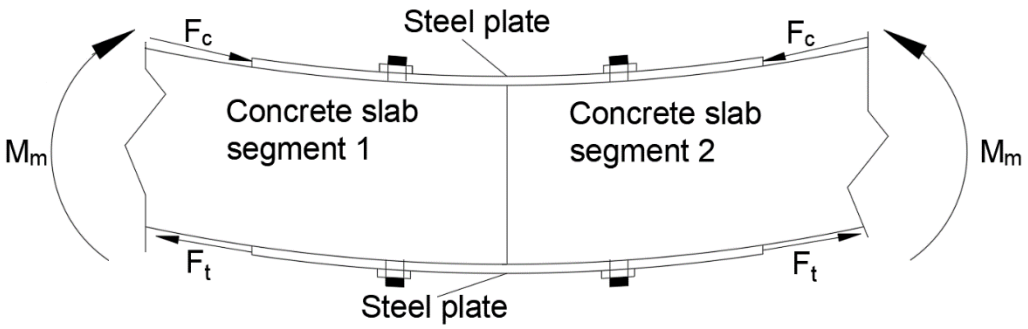

a. Force transfer through steel plates

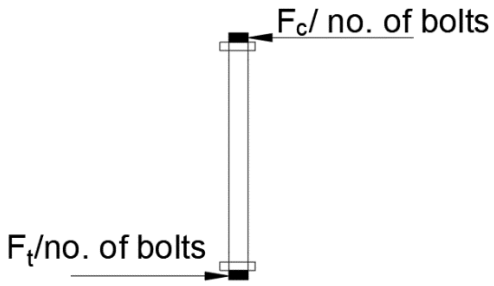

b. Force transfer through steel bolts

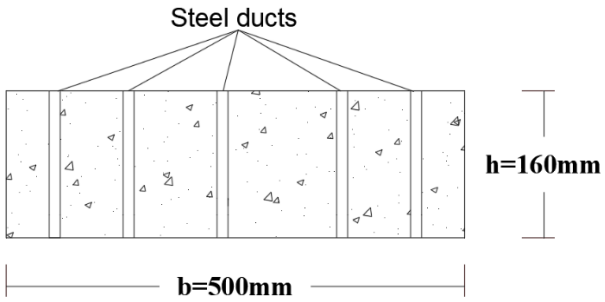

c. Details of net section area of concrete along the bolt line (no steel blocks)

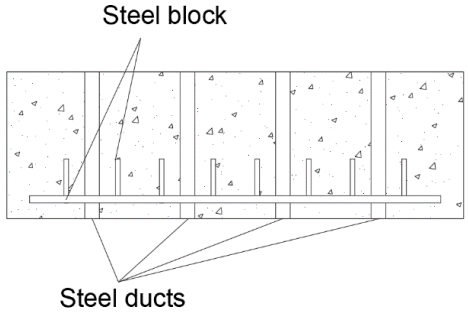

d. Details of net section area of concrete along the bolt line (with steel blocks)

Figure 19: Forces transformation in demountable slabs.

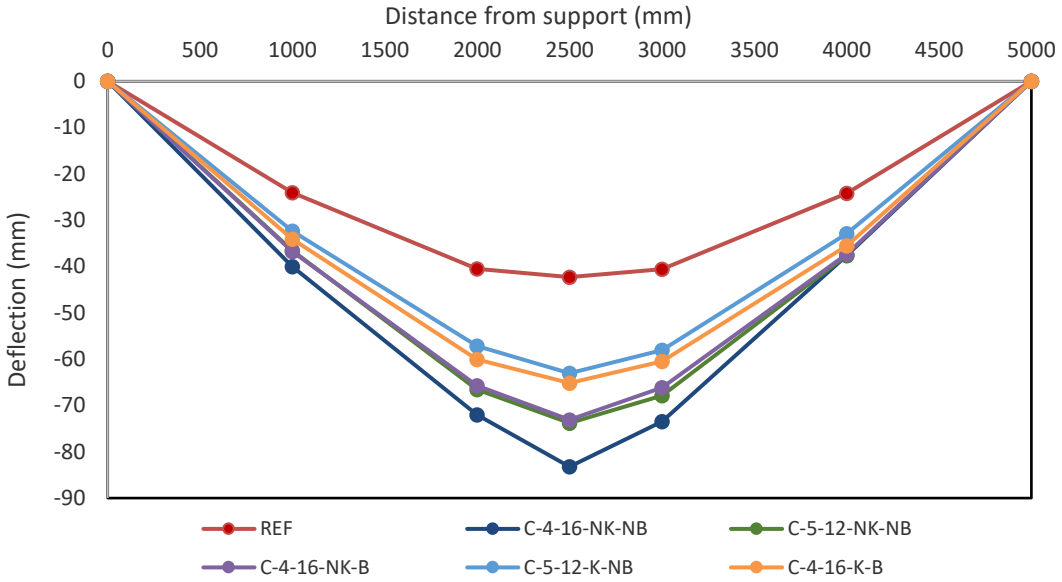

Figure 20: Deflection profile of tested slabs at 15 kN of the total load.

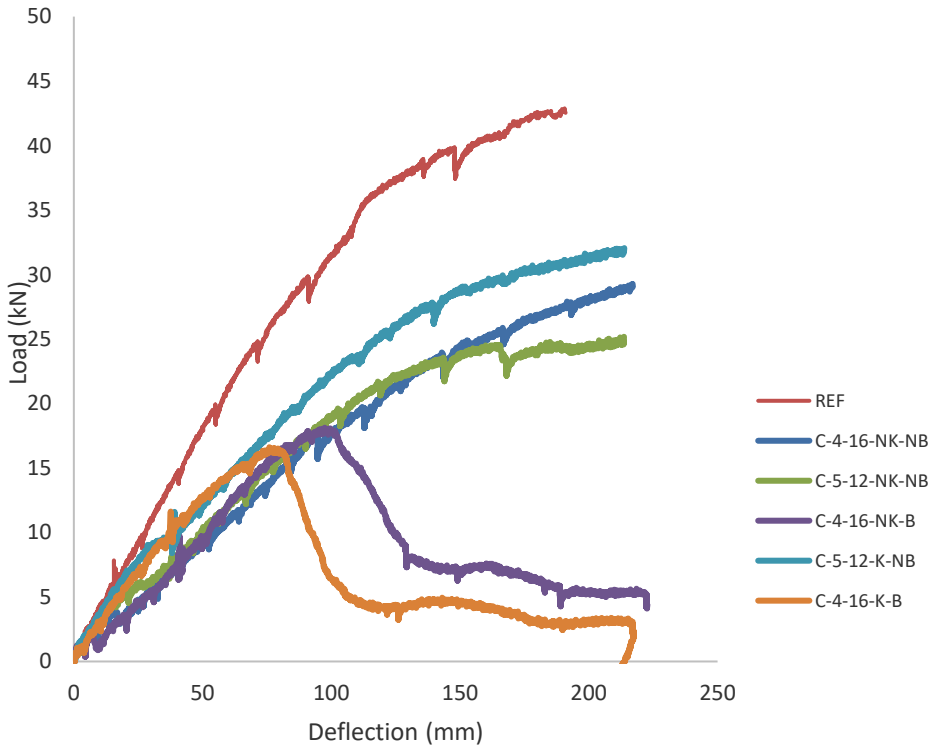

Figure 21: Load-deflection behaviour at the mid-span section.

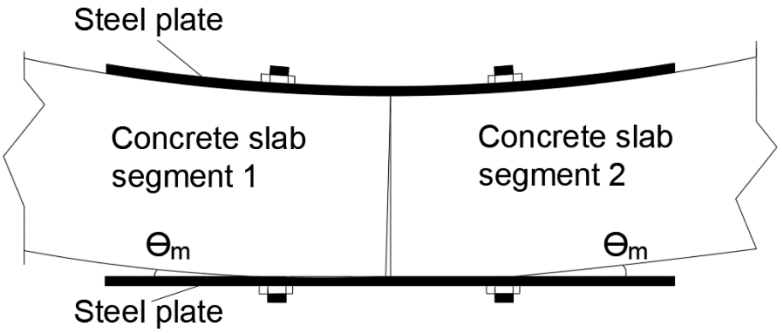

Figure 22: Rotation at midspan to the left or right of the demountable connection.

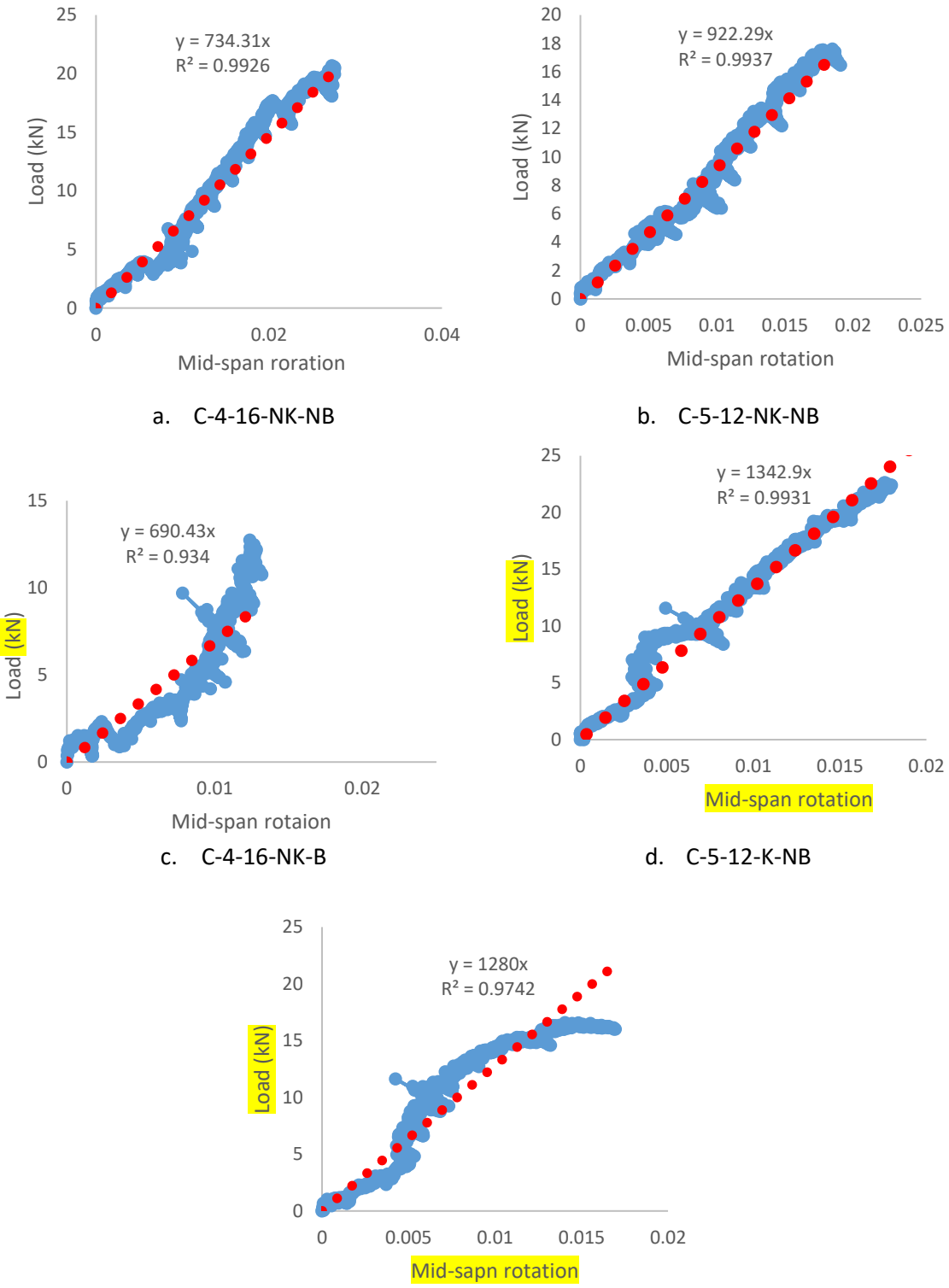

Figure 23: Linear regression between the total experimental load and the mid-span rotation values.

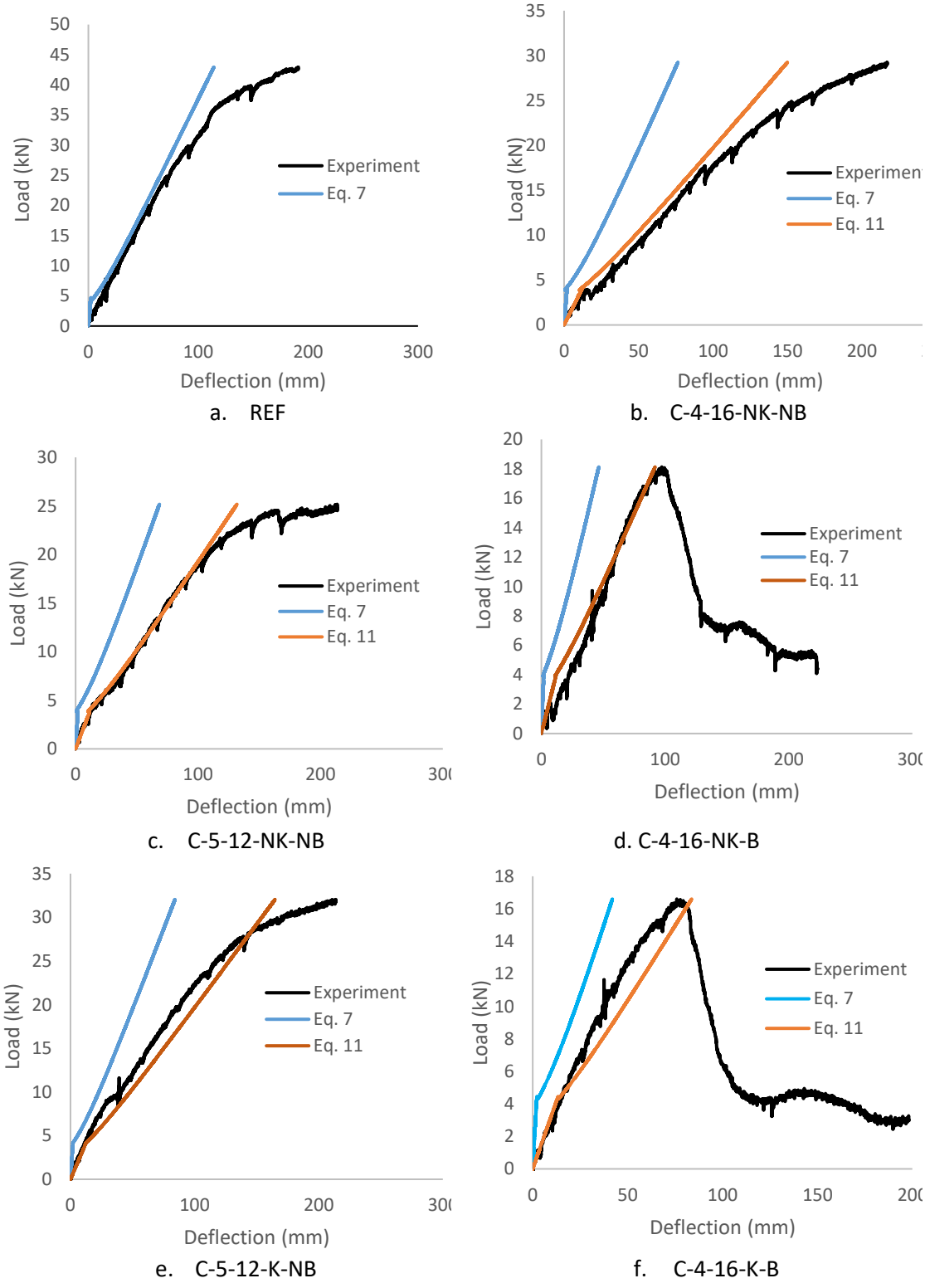

Figure 24: Comparison between the predicted and the experimental load deflection behaviour

6. Tables

Table 1: Details of dry connections of the tested specimens.

slab notation	key at the connection	embedded steel block	number of parts	equal parts	number of bolts diameter	bolts diameter (mm)
REF	-	-	-	-	-	-
C-4-16-NK-NB	no	no	2	yes	4	16
C-5-12-NK-NB	no	no	2	yes	5	12
C-4-16-NK-B	no	yes	2	yes	4	16
C-5-12-K-NB	yes	no	2	no	5	12
C-4-16-K-B	yes	yes	2	no	4	16

Table 2: Mechanical properties of the reinforcement bars

Bar size	Area (mm2)	Yielding strength (MPa)	Ultimate strength (MPa)	Modulus of elasticity (GPa)	Ultimate strain %
12 mm	113.1	574	784	143	0.14
8 mm	50.3	700	851	139	0.14

Table 3: Concrete properties for the tested slabs.

slab notation	f_{cu} (MPa)	f_c'(MPa)	f_{ts} (MPa)
REF	43.7	37.2	1.96
C-4-16-NK-NB	47.7	40.5	1.96
C-5-12-NK-NB	43.4	36.9	1.96
C-4-16-NK-B	45.2	38.42	2.13
C-5-12-K-NB	46.7	39.7	2.13
C-4-16-K-B	46.5	39.5	2.13

Note: f_{cu} is the cube compressive strength, f_c' is the equivalent cylinder compressive strength assumed to be equal to $0.85f_{cu}$, f_{ts} is the concrete tensile strength.

Table 4: Crack width, total failure load and theoretical capacity predictions of the tested slabs.

Slab notation	Theoretical cracking load	Crack width (mm)		Total load (kN)	Predicted moment capacity (kNm)	Ratio of experimental/ predicted moment capacities
		At max load	At max actuator deflection			
REF	4.18	1.01	1.01	42.9	40.16	1.07
C-4-16-NK-NB	4.18	5.9	5.9	29.3	21.8	1.34
C-5-12-NK-NB	4.18	13.5	13.5	25.2	21.0	1.20
C-4-16-NK-B	4.54	0.71	14.3	18.13	17.2	1.05
C-5-12-K-NB	4.54	9.0	9.0	32.07	20.8	1.55
C-4-16-K-B	4.54	2.03	21.4	16.62	17.5	0.95

Table 5: Relationship between the experimental load and mid-span rotation based on the best linear regression

Slab notation	mid-span rotation, θ_m
C-4-16-NK-NB	$\theta_m = (2/734.31)\mathrm{P}$
C-5-12-NK-NB	$\theta_m = (2/922.29)\mathrm{P}$
C-4-16-NK-B	$\theta_m = (2/690.43)\mathrm{P}$
C-5-12-K-NB	$\theta_m = (2/1342.9)\mathrm{P}$
C-4-16-K-B	$\theta_m = (2/1280)\mathrm{P}$

Table 6: Pearson correlation coefficient computed using the experimental rotation and experimental load

Slab notation			Rotation	Load
C-4-16-NK-NB (N=2271)	Rotation	Pearson Correlation	1	.983**
		Sig. (2-tailed)		.000
	Load	Pearson Correlation	.983**	1
		Sig. (2-tailed)		
C-5-12-NK-NB (N=3759)	Rotation	Pearson Correlation	1	.862**
		Sig. (2-tailed)		.000
	Load	Pearson Correlation	.862**	1
		Sig. (2-tailed)	.000	
C-4-16-NK-B (N=1358)	Rotation	Pearson Correlation	1	.913**
		Sig. (2-tailed)		.000
	Load	Pearson Correlation	.913**	1
		Sig. (2-tailed)	.000	
C-5-12-K-NB (N=1559)	Rotation	Pearson Correlation	1	.99**
		Sig. (2-tailed)		.000
	Load	Pearson Correlation	.99**	1
		Sig. (2-tailed)	.000	
C-4-16-K-B (N=1324)	Rotation	Pearson Correlation	1	.948**
		Sig. (2-tailed)		.000
	Load	Pearson Correlation	.948**	1
		Sig. (2-tailed)	.000	

**. Correlation is significant at the 0.01 level (2-tailed). N: is the sample size.